



Asteroseismology Applied to Constrain Structure Parameters of δ Scuti Stars

Subrata Kumar Panda¹, Siddharth Dhanpal¹ , Simon J. Murphy² , Shравan Hanasoge¹ , and Timothy R. Bedding³ ¹Department of Astronomy and Astrophysics, Tata Institute of Fundamental Research, Colaba, Mumbai 400005, Maharashtra, India²Centre for Astrophysics, University of Southern Queensland, Toowoomba, QLD 4350, Australia³Sydney Institute for Astronomy (SfA), School of Physics, University of Sydney, NSW 2006, Australia

Received 2023 June 6; revised 2023 September 10; accepted 2023 September 25; published 2024 January 2

Abstract

Asteroseismology is a powerful tool to probe stellar structure. Spaceborne instruments like CoRoT, Kepler, and TESS have observed the oscillations of numerous stars, among which δ Scutis are particularly interesting, owing to their fast rotation and complex pulsation mechanisms. In this work, we inferred model-dependent masses, metallicities, and ages of 60 δ Scuti stars from photometric, spectroscopic, and asteroseismic observations using least-squares minimization. These statistics have the potential to explain why only a tiny fraction of δ Scuti stars pulsate in a very clean manner. We find most of these stars with masses around $1.6 M_{\odot}$ and metallicities below $Z = 0.010$. We observed a bimodality in age for these stars, with more than half the sample younger than 30 Myr, while the remaining ones were inferred to be older, i.e., hundreds of Myrs. This work emphasizes the importance of the large-frequency separation ($\Delta\nu$) in studies of δ Scutis. We also designed three machine-learning (ML) models that hold the potential for inferring these parameters at lower computational cost and much more rapidly. These models further revealed that constraining dipole modes can help in significantly improving age estimation and that radial modes succinctly encode information regarding luminosity and temperature. Using the ML models, we also gained qualitative insight into the importance of stellar observables in estimating mass, metallicity, and age. The effective temperature T_{eff} strongly affects the inference of all structure parameters, and the asteroseismic offset parameter ϵ plays an essential role in the inference of age.

Unified Astronomy Thesaurus concepts: [Delta Scuti variable stars \(370\)](#)

Supporting material: figure set

1. Introduction

Asteroseismic observations from TESS (Ricker et al. 2014) and Kepler (Borucki et al. 2010) have shed light on the dynamics and interiors of thousands of pulsating stars (Paparó 2019; Bowman 2020; Aerts 2021; Kurtz 2022). A sizeable fraction of the pulsating class from these missions are δ Scuti (hereafter δ Sct; Bowman et al. 2018; Guzik 2021) stars, which lie at the junction of the instability strip and the main-sequence (MS) band in the Hertzsprung–Russell (H-R) diagram (Uytterhoeven et al. 2011), providing direct views of both these classes. These are low-to-intermediate-mass (1.5 – $2.5 M_{\odot}$) MS variables with spectral types ranging from A to F (Bowman et al. 2018; Murphy 2021; Kurtz 2022). High-amplitude δ Sct stars are used as standard candles (McNamara et al. 2007) and in assessing the metallicities and ages of stellar clusters (Murphy et al. 2022), in turn enabling Galactic archeology.

Asteroseismology is a powerful tool that can be used to estimate various structure parameters such as mass, composition, and age on different pulsating classes, e.g., stochastic oscillators (Chaplin et al. 2013; Vrard et al. 2016; Hekker & Christensen-Dalsgaard 2017; Hon et al. 2017, 2018; Dhanpal et al. 2022), γ -Doradus stars (Li et al. 2019; Mombarg et al. 2021), and high-mass coherent oscillators (Hendriks et al. 2019), among others. Some effort has been applied to similar studies of δ Sct stars (Suárez et al. 2014; García Hernández et al. 2017; Barceló Forteza et al. 2020; Pamos Ortega et al. 2022). In this paper, we develop a

methodology to measure structure parameters—mass, metallicity, and ages of δ Sct stars. These measurements can in principle constrain the metallicities and ages of the host open clusters from which these stars formed and were dispersed before escaping to become field stars.

δ Sct stars predominantly exhibit low radial-order pulsations, with high-frequency pressure and low-frequency gravity modes, roughly separated around 5 d^{-1} , although this depends on T_{eff} to leading order (Moya et al. 2017). The pressure modes are mainly driven by the κ mechanism (Chevalier 1971) in the helium ionization zone. They primarily propagate in the stellar envelope and probe the near-surface regions.

Although we have precise estimates of the luminosity (L), effective temperature (T_{eff}), and pulsation frequencies, the seismology and the parameter inference of δ Sct stars are challenging because of the following reasons: (a) they have low radial-order p -modes and g -modes, where asymptotic theory fails; (b) many stars exhibit fast rotation, leading to ellipsoidal deformation (Reese et al. 2006); (c) complex mode-selection mechanisms (Dziembowski et al. 1990) influence the observed spectra; and (d) appearance of island modes (Reese et al. 2006), chaotic modes (Barceló Forteza et al. 2017), etc., make it very difficult to characterize δ Sct spectra.

Finding regular patterns in δ Sct spectra is very helpful for carrying out asteroseismology. Although some δ Sct stars had been previously reported to show regular frequency spacings (Mathews 2007; García Hernández et al. 2009; Zwintz et al. 2011; Paparó et al. 2013; Suárez et al. 2014), a larger ensemble of such stars was found by Bedding et al. (2020), who identified 60 δ Sct stars from TESS and Kepler exhibiting regular pulsation patterns. They were able to identify some modes, label their radial orders, and deduce the large-frequency separation ($\Delta\nu$) and p -

mode offset (ϵ). Many more examples of high-frequency patterns in δ Sct stars have subsequently been identified (e.g., Murphy et al. 2020, 2021, 2022; Hasanzadeh et al. 2021; Le Dizès et al. 2021; Kahraman Alicavus et al. 2022). Here, we use seismic parameters to infer stellar structure through the application of neural networks and other techniques. As the relationships between observables such as luminosity, temperature, pulsation frequencies, and structure parameters can be highly nonlinear, neural networks can potentially be useful in building a model connecting them all. In addition, a well-trained neural network infers these structure parameters substantially faster than conventional methods such as Markov Chain Monte Carlo, making it a capable method for ensemble studies.

At the core of this work lie the simulated models of δ Sct stars, which we briefly describe in Section 2. Following that we elaborate on developing three different machine-learning (ML) methods in Section 3, which in principle could have inferred mass, metallicity, and ages of δ Sct stars. However, none of the above methods worked uniformly well over all the stars in our sample because of various limitations. Yet, the networks helped us in gaining qualitative insights into the importance of different observables, which we present along with each method. Since our goal was to characterize the 60 δ Sct stars from Bedding et al. (2020), we finally deployed a grid-search-based least-squares minimization technique in Section 4, with which we were able to infer (M , Z , τ) parameters for all stars. We end the article with presenting the statistics of these inferences. While we have presented all the ML-based methods for the sake of completeness, we found that the least-squares fitting method performed best and therefore regard its output as our final result.

2. Grid of Stellar Models

We have used the model grid presented in Murphy et al. (2023), which contains more than 800,000 stellar models. However, since we aimed for training the networks on δ Sct stars, we extracted 524,247 models based on a simpler criterion of $6500 \text{ K} \leq T_{\text{eff}} \leq 10,000 \text{ K}$. MESA inlists used for the grid computation and the corresponding output models are available as supplementary files in Murphy et al. (2023). This grid covers a wider span of mass (M) and metallicity (Z) over the ranges $[1.3\text{--}2.2] M_{\odot}$ and $[0.002\text{--}0.026]$, with $0.1 M_{\odot}$ (M) and 0.002 (Z) resolution, respectively.

These models were evolved using the stellar evolution code MESA (Paxton et al. 2010, 2013, 2015, 2018, 2019), and corresponding pulsation frequencies were calculated using GYRE (Townsend et al. 2013, 2017; Goldstein et al. 2020)—which in turn provides the large-frequency separation ($\Delta\nu$) and offset parameter (ϵ).

The computed eigenmodes comprise p -, g -, and mixed modes oscillating at frequencies between 0 to 95 d^{-1} and at harmonic degrees of $\ell = 0$ and 1. Since the majority of δ Sct stars pulsate in radial and dipole modes, and higher-degree modes are not observable due to geometric cancellation, the availability of modes with degree $\ell = 2$ or higher is not necessary for our purpose. All the computed modes correspond to nonrotating $m = 0$ components. $\Delta\nu$ and ϵ were calculated by fitting the asymptotic relation to radial ($\ell = 0$) p -modes with order (n_{pg}) larger than 5.

We used this grid to train the neural networks to infer structure parameters from observables and asteroseismic quantities.

The H-R diagram (Figure 1) shows the stellar models, including the potential δ Sct models ($3.83 \leq \log T_{\text{eff}} \leq 4$) on this H-R

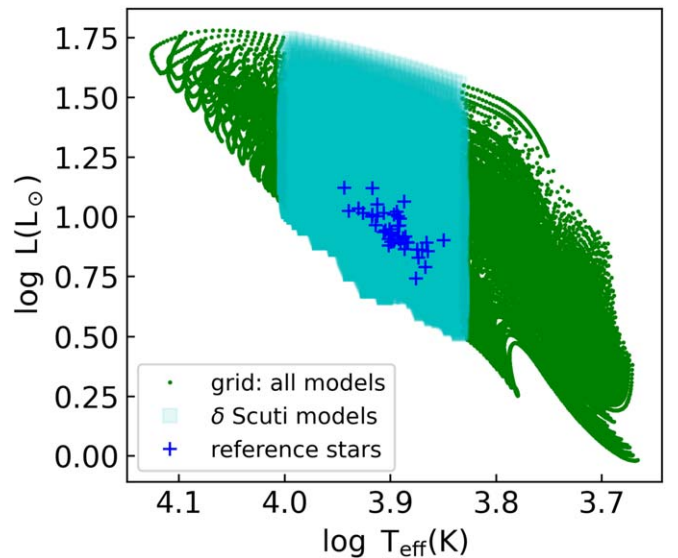


Figure 1. H-R diagram showing the positions of all synthetic stellar models, with δ Sct stars present in the solid patch. The δ Sct targets of this paper are denoted using plus sign symbols.

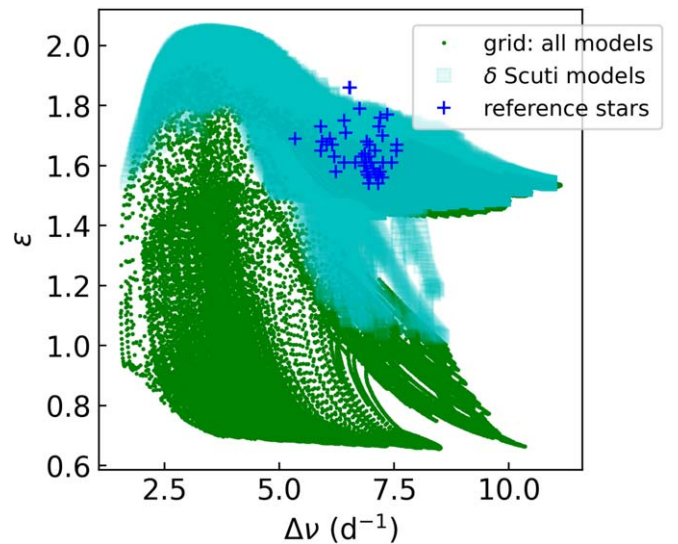


Figure 2. $\Delta\nu - \epsilon$ diagram denoting the positions of all synthetic stellar models, with δ Sct stars present in the solid patch. The δ Sct targets of this paper are denoted using plus sign symbols.

diagram. For reference, we mark the target stars of this work using plus sign symbols, which are taken from the observed δ Sct stars in Bedding et al. (2020). Figure 2 contains the same models as Figure 1 but shows the asteroseismic $\Delta\nu - \epsilon$ diagram. Both figures demonstrate that the phase space of our stellar grid is broad enough to represent the wide range of observed δ Sct stars.

3. Machine-learning-based Methods

The application of ML algorithms to the fitting of stellar models has shown great promise (Verma et al. 2016; Hendriks et al. 2019; Dhanpal et al. 2022; Scutt et al. 2023). For the work presented in this article, we have developed three different versions of neural networks that perform regression to infer the values of M , Z , and age (τ). Our networks were developed using the Python libraries TENSORFLOW (Abadi et al. 2015) and KERAS (Chollet et al. 2015).

In each set of ML experiments, we randomly split the δ Sct model grid into “training” and “test” (validation) data at a 95: 5 ratio. The network used the training data to learn different features and compute the output. The training aimed to minimize the loss function by reducing the mean-squared error between the actual and predicted outputs (Equation (1)) through stochastic gradient descent:

$$\text{MSE} = \sum_{i=1}^N \frac{(y_{\text{predicted}}^i - y_{\text{true}}^i)^2}{N}. \quad (1)$$

The training takes place through a back propagation technique that gradually optimizes the network parameters using the ADAM optimizer (Kingma & Ba 2014). To avoid the situation where networks memorize the data set instead of learning the inherent features, we equipped the output layer of each network with an L2 regularizer having regularizing parameter $\lambda = 10^{-6}$.

Once the training is over, we validated network accuracy on the unseen test data and also compared the network prediction against ground truth. If the accuracy and the comparison were deemed acceptable on the validation data, we concluded that the network was successfully trained without overfitting.

We used the cross-validation method (Mosteller et al. 1968) to yield a distribution of 40 instances of inferences from trained network of which median, 16th, and 84th percentiles were calculated to obtain the most probable result and lower and higher uncertainties.

However, these three networks were not able to yield meaningful inferences over real stars due to several limitations discussed below. Nonetheless, they have the potential to provide qualitative insights on relative importance of different observables in the way (Bellinger et al. 2016) assessed for MS stars. We performed this analysis for all the three networks. Physical interpretation of such analysis is also presented.

3.1. Method 1: ML Using Seismic Indices

In this method we deployed three regression networks to infer M , Z , and τ from four input parameters: $\{L, T_{\text{eff}}, \Delta\nu, \epsilon\}$. Although radius (R) is dependent on L and T_{eff} , supplementing it as an additional input helped the networks train quickly and achieve higher accuracy.

For the network to infer age (τ), it typically requires prior knowledge of M and Z : this is because each physical parameter (θ) is a function of M , Z , and τ , which is why age inversion requires (M , Z) to be supplied as inputs:

$$\theta = f(M, Z, \tau) \implies \tau = \tilde{f}^{-1}(M, Z, \theta).$$

The network architecture comprised of 1 input layer (with 5–7 neurons), 10 intermediate layers (of 400 neurons each), and 1 single-neuron output layer (Figure 3). With the exception of the output layer, which has a \tanh activation function, all other neurons were activated using the rectified linear unit function. Since we developed a few alternative methods, we label this procedure as *Method-1* for easy reference.

We trained the networks and compared the network-predicted values for the validation data with the corresponding true values (Figure 4). The network was able to achieve high accuracy in predictions of M and Z . Figure 5 shows the distributions of errors in our predictions on the validation data.

From Figure 4(c), it is evident that while age inferences are accurate for younger ($\log \tau/\text{Myr} < 1$) and older stars

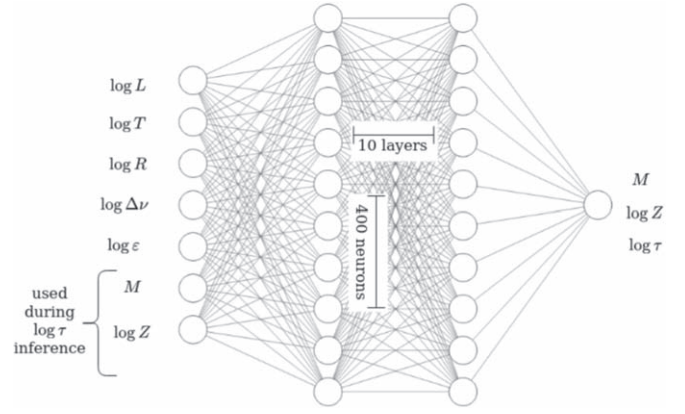


Figure 3. Architecture of the neural-network models.

($\log \tau/\text{Myr} > 2.5$), the network systematically overpredicts for stars of intermediate age ($\log \tau/\text{Myr} \sim 1.3\text{--}2.5$). A possible reason for this discrepancy is that no observable evolves as a monotonic function of age. All structure and seismic parameters cross their pre-MS values sometimes within the MS, as shown in Figure 6. Hence, none of our inputs may be used to uniquely distinguish between two possible ages. This fact was also discussed in Murphy et al. (2021a).

We implemented our trained networks on 43 δ Sct stars from Bedding et al. (2020), for which T_{eff} , L , $\Delta\nu$, and ϵ measurements were simultaneously available. While investigating the results, we noticed that most of the inferences have unusually high metallicity of $Z = 0.026$, which is also the upper boundary of our model grid. It is well-known that what the neural networks learn is not easily interpretable (Montavon et al. 2018). This makes it impossible to investigate and mitigate the shortcomings with the method.

3.1.1. Feature Importance

We determined the qualitative importance of various inputs to determine how strongly they influence parameter estimation. To measure the independent contributions arising from the inputs, we perturbed each input quantity by 0.5% (without changing other inputs) and measured the relative differences in outputs. We expected the contribution of the input to be proportional to the relative difference in output. We carried out this process for all input quantities to determine their qualitative importance. Figure 7 shows the average relative differences, which can be taken as a proxy for feature importance.

Figure 7 indicates that $\log T_{\text{eff}}$ contributes the most toward the inference of all parameters. T_{eff} is strongly influenced by the conditions at the stellar core (T_c) through various transport and mixing processes. Hence, stellar age, which strongly depends on core hydrogen abundance (X_c), can be expected to correlate with T_c and hence indirectly with T_{eff} .

M and Z are necessary inputs for the inference of age, which is straightforward from the inversion relation discussed above. Despite being an offset parameter that controls the shift in the $\ell = 0$ frequencies, ϵ plays an important role in the inference of τ . This was also emphasized in Bedding et al. (2020), where the $\Delta\nu - \epsilon$ diagram was shown to encode information about age (τ).

Apart from T_{eff} , M significantly depends on L , which is likely due to the well-known “mass–luminosity” relation. Its dependence on $\Delta\nu$ is not surprising, owing to the fact that M is related to density (ρ) and $\Delta\nu \propto \sqrt{\rho}$.

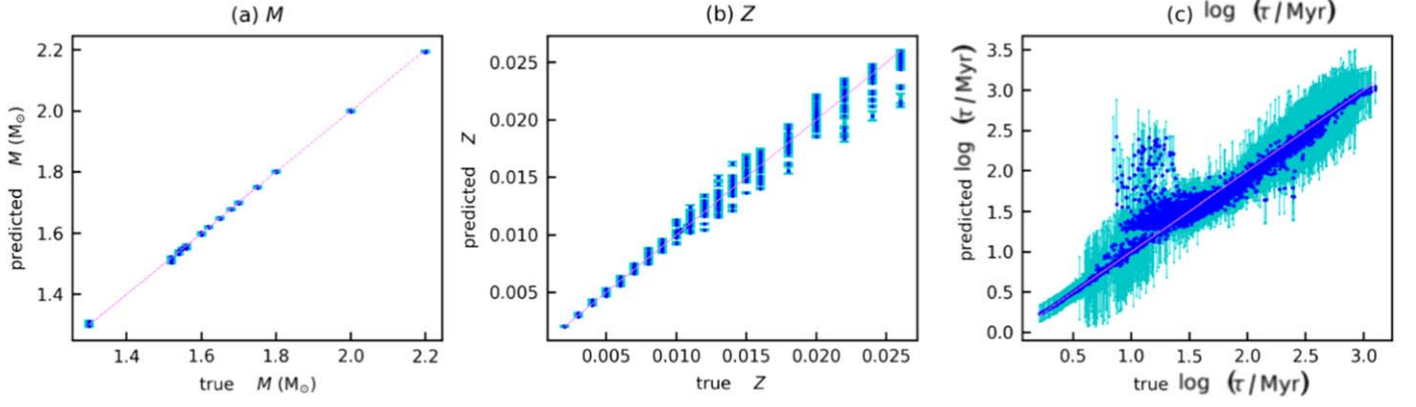


Figure 4. Plots showing network predictions for validation samples against their corresponding true values. Shown for (a) M , (b) Z , and (c) $\log \tau$. Uncertainties associated with predicted values are also shown.

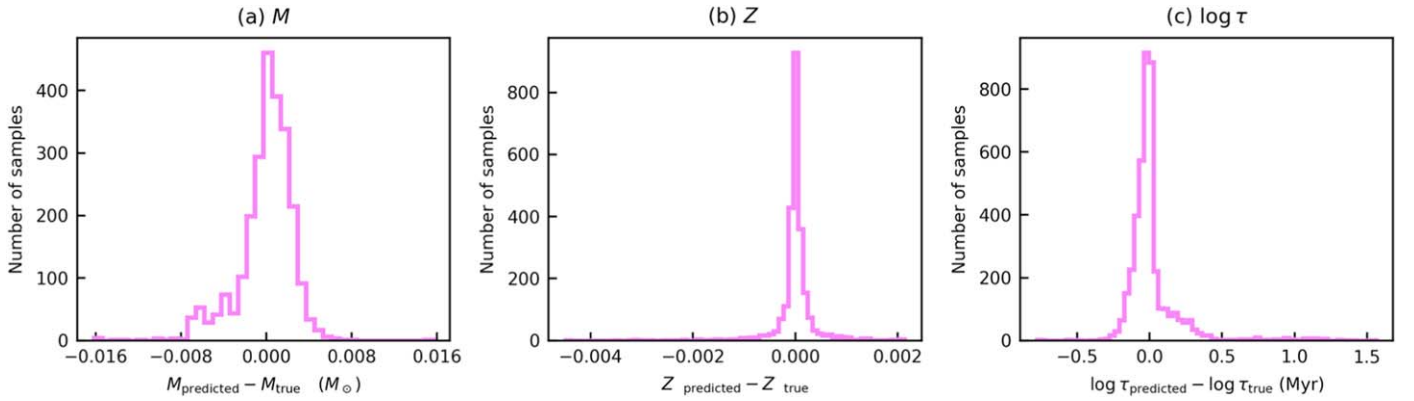


Figure 5. Distribution of errors between network predictions for validation samples and their corresponding true values: shown for (a) M , (b) Z , and (c) $\log \tau$.

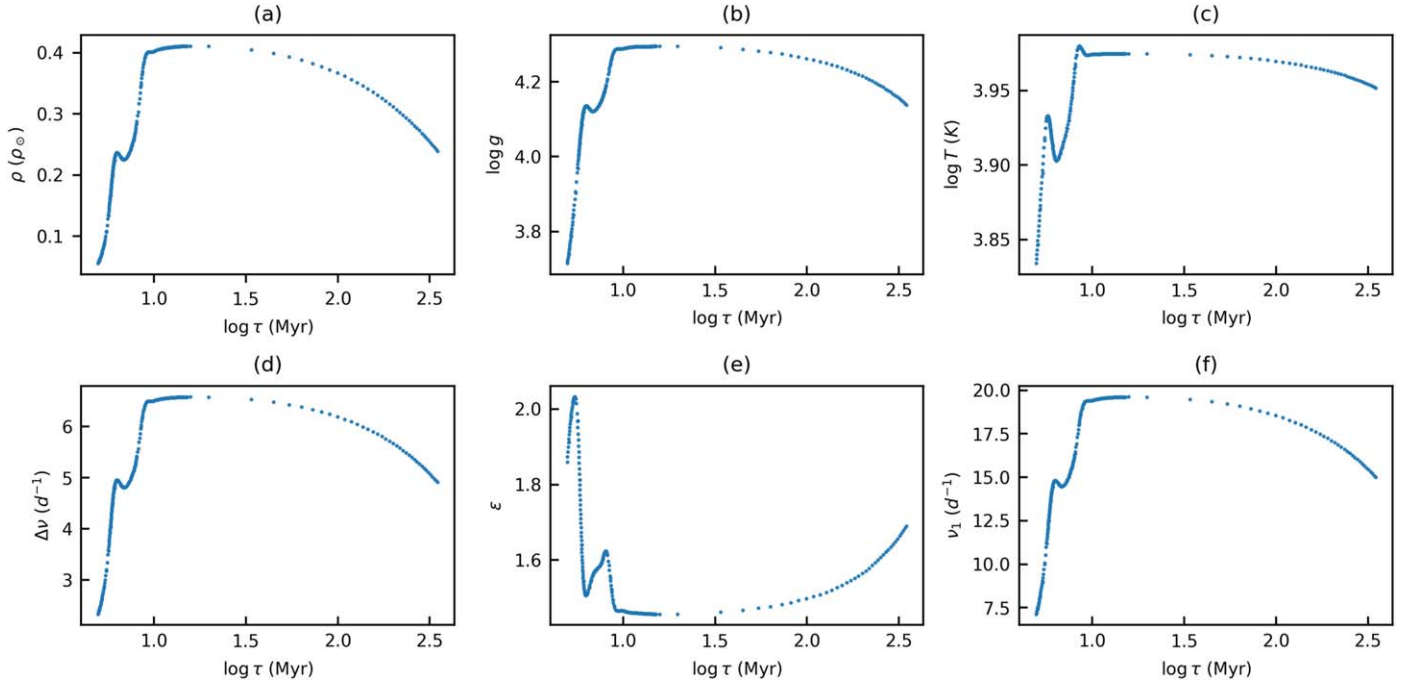


Figure 6. Evolution with time of stellar properties for a model with mass $2.2 M_{\odot}$ and $Z = 0.026$. Most structural and seismic quantities cross their pre-MS values during MS. Hence, values of these parameters are degenerate at two different ages. Crossing effects are shown for (a) ρ , (b) $\log g$, (c) $\log T_{\text{eff}}$, (d) $\Delta \nu$, (e) ϵ , and (f) ν_1 (frequency corresponding to $n = 1, \ell = 0$).

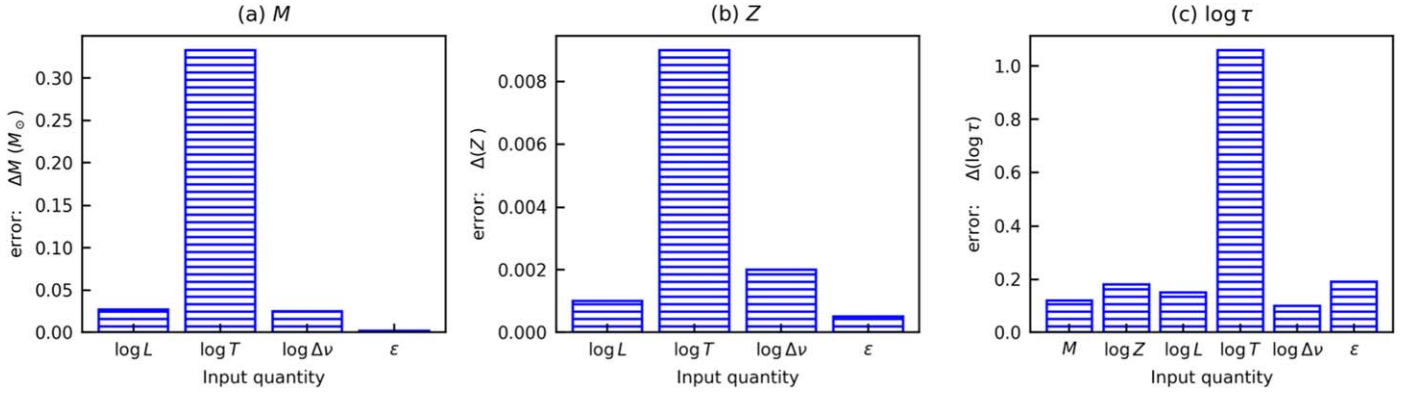


Figure 7. Different inputs contribute unequally toward overall inferences of (a) M , (b) Z , and (c) $\log \tau$. This figure qualitatively depicts the contribution strengths corresponding to the input parameters when perturbed by 0.5%.

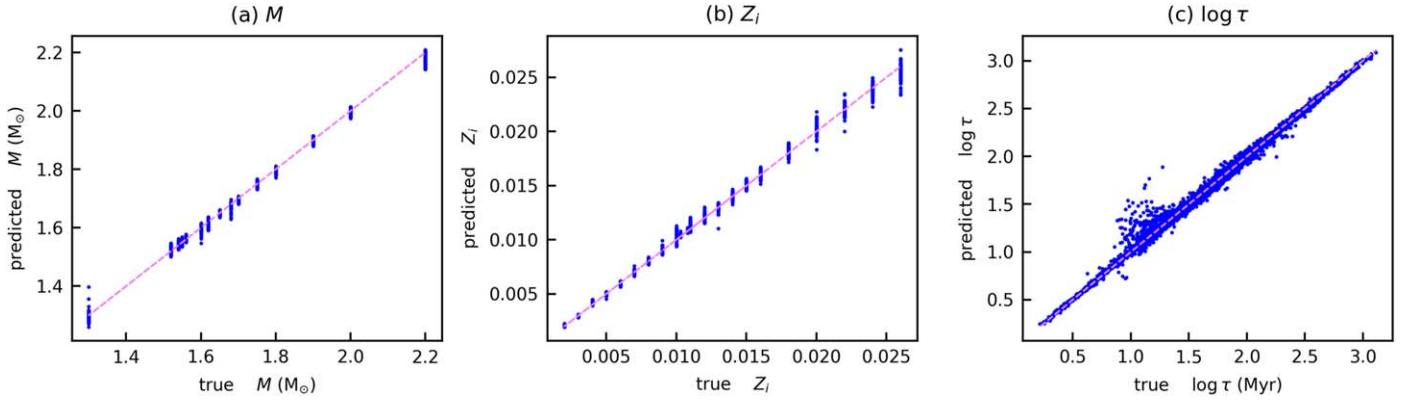


Figure 8. Network predictions for validation samples for (a) M , (b) Z_i , and (c) $\log \tau$, on taking eigenfrequencies $\{\nu_1, \dots, \nu_7\}$ as inputs (without L , T_{eff} , $\Delta\nu$, ϵ). This implies that these non-asymptotic modes are helpful for parametric inference and particularly useful when L or T_{eff} is not available or reliable.

$\Delta\nu$ plays an important role in the inference of Z . It is highly correlated with the square root of mean stellar density—which is tightly related to metallicity (Z) because the higher the metallicity, the lower the stellar density.

3.2. Method 2: ML Using Radial Modes

Although we used L as an input quantity in Method-1, the reliability of its measurements depends on the accuracy of stellar distance, as L is calculated using magnitude and distance. Since structure parameters are very sensitive to $\log T_{\text{eff}}$ (evident from Section 3.1.1), errors in measuring the latter propagate into inferences of the former.

In this section, we show that if we use the first seven eigenfrequencies of radial-mode oscillations instead of the observables (L , T_{eff} , $\Delta\nu$, ϵ), we still achieve similar results while overcoming existing issues. The reason behind such selection is that (i) all the synthetic models at least possess seven overtones of radial modes and (ii) radial modes are far more easily identifiable than dipole modes using period ratios (Petersen & Christensen-Dalsgaard 1996) and multicolor photometry-like (Garrido et al. 1990) techniques.

Architecture and training of this network are similar to those of Method-1, except its input layer comprises of seven neurons to accept the seven radial modes.

In this formalism, neural networks could learn all the parameters, even without needing $\{L, T_{\text{eff}}, \Delta\nu, \epsilon\}$, as seen in Figure 8. We compare the average learning accuracy (=100% - average% error) associated with each parameter inference using the current method and Method-1 of Section 3.1. This method

is as accurate as Method-1 in inferring M and Z . However, it

Table 1
Comparing Performances between Neural Network–Based Method-1 and Method-2

Inputs:	Method-1 (Section 3.1) (L , T_{eff} , $\Delta\nu$, ϵ) (%)	Method-2 (Current Method) ($\{\nu_1 - \nu_7\}$) (%)
M	99.9	99.5
Z	99.7	99.5
$\log \tau$	93	96

Note. While both perform similarly, Method-2 works without $\{L, T_{\text{eff}}, \Delta\nu, \epsilon\}$.

infers age at a significantly higher accuracy (Table 1). We designate this procedure as Method-2 in order to distinguish it from Method-1.

This method highlights the importance of the $\ell=0$ eigenfrequencies of radial orders $n=1-7$. It shows that the non-asymptotic modes succinctly preserve the representation of L and T_{eff} although how this is so is unclear.

Despite its robustness, we were unable to apply this method to the observed stars since accurately identifying continuous radial overtones ($\nu_1 - \nu_7$) is difficult. Additionally, it was harder to automate this method for multiple stars because identifying radial orders requires significant human intervention. Identifying radial modes crucially depends on choosing the correct $\Delta\nu$, without which échelle diagrams cannot be

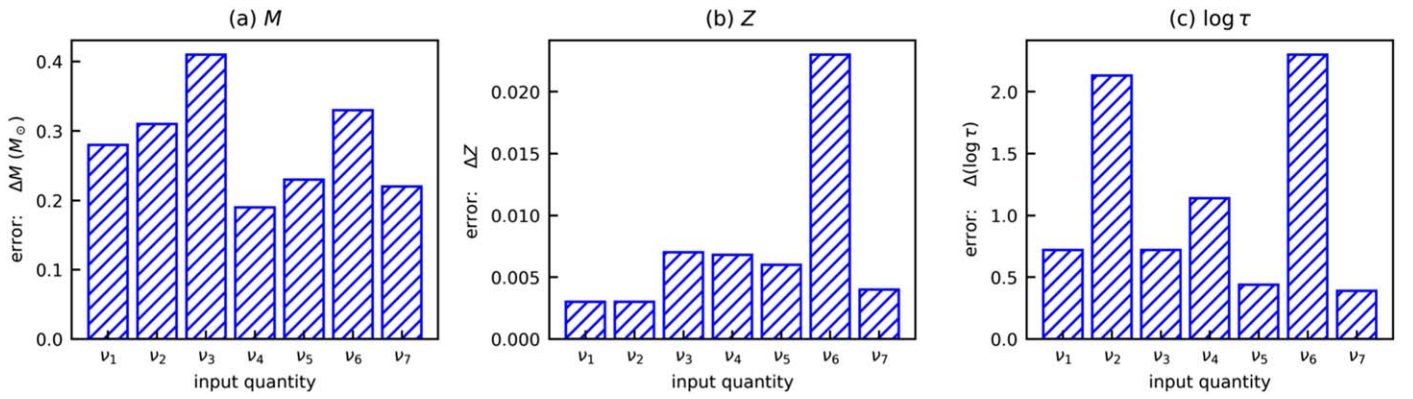


Figure 9. Importance of the first seven eigenfrequencies in the inference of (a) M , (b) Z , and (c) $\log \tau$.

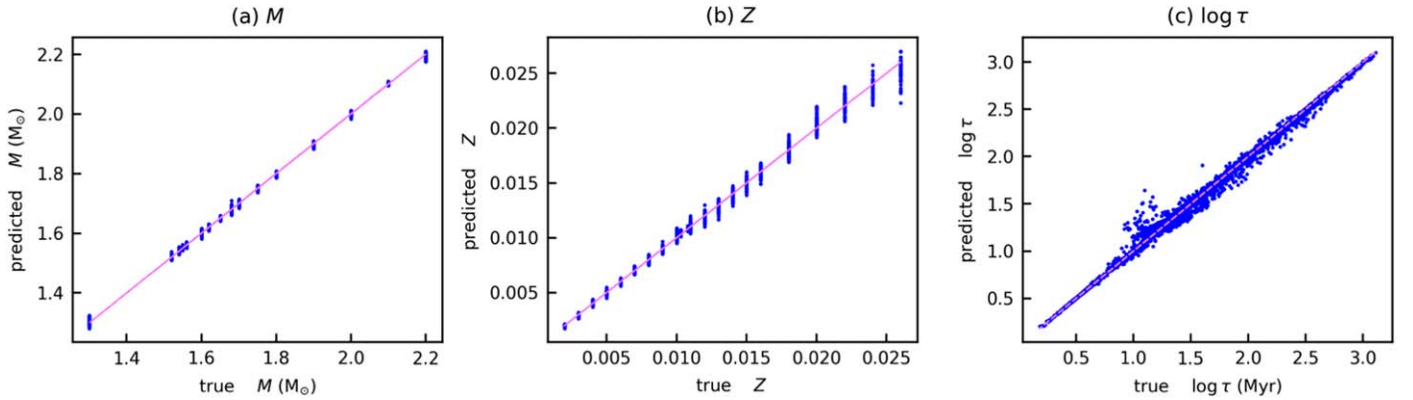


Figure 10. Improved network prediction after inputting radial-dipole ($\ell = 0, 1$) modes of overtone $n \in [4-7]$ along with $\{L, T_{\text{eff}}\}$. The age inference is much more accurate than the approaches described earlier.

constructed. Even if this method worked efficiently, we were unable to resolve the age discrepancy (similar as Method-1) over the synthetics, as evident from Figure 8(c). In Section 3.3, we propose another method that improves over this issue.

3.2.1. Feature Importance

We investigated the strengths of contributions arising from each mode involved in the inference routine. We measured their importance in a manner similar to that in Section 3.1.1. The attendant measures are shown in Figure 9. It may be understood from the figure that all frequencies are not equally important. ν_6 has the highest contribution, followed by ν_2 and ν_3 . Hence, both non-asymptotic and asymptotic modes seem to be important.

It is surprising that the network depends so significantly on ν_6 , which is robust over a range of different $\Delta\nu$ and ϵ . The probable cause is that the transition to asymptotic nature ($n \gg \ell$) from low-order non-asymptotic modes occurs around ν_6 . It is possible that ν_6 therefore contains information from both regimes.

Having emphasized the salient features of ν_6 , it is interesting that the network does not equally depend on modes of radial order 4, 5, and 7—which altogether constitute the asymptotic series and hence carry similar $\Delta\nu$ characteristics. This may be similar to principal component analysis or dimensionality reduction algorithms, and the network is trying to rely on as few inputs as possible, leaving others redundant.

3.3. Method 3: ML Using Radial and Dipole Modes

In this section, we present the final follow-up experiment to study the importance of dipole modes. Every experiment carried out so far has dealt with radial ($\ell = 0$) modes or quantities such as $\{\Delta\nu, \epsilon\}$ that depend on radial modes. However, since dipole modes are often seen in échelle diagrams (Bedding et al. 2020) of δ Sct stars, it is useful to conduct these experiments in order to study their contribution.

In this method, we built a model that took observables $\{L, T_{\text{eff}}\}$ and eigenfrequencies with $n \in [4-7]$ from each of the $\ell = 0$ and 1 ridges and produced as output the structure parameters. For age inference, we supplemented pre-inferred M and Z to the frequencies and $\{L, T_{\text{eff}}\}$. We refer to this procedure as Method-3.

Figure 10 and Table 2 indicate that the networks were able to learn M , Z , and $\log \tau$ from synthetics and the accuracy of age inference has improved. Since the current method adequately constrains age, this emphasizes the importance of dipole modes.

With more number of inputs to neural network, it is supposed to gain higher accuracy. We also measured χ^2/N for all the three experiments to assess which method is more efficient. Here χ^2 mean average squared differences between true and machine-predicted values and N represent the number of inputs fed to the networks. Table 3 summarizes these facts.

We observe that Method-2 consistently outperforms Method-1. Method-3 excels among all of these but for age inference it could not outperform Method-2. This may be due to the relatively larger (yet tolerable) spread at larger ages compared to Method-2. Global

Table 2
Comparing Performances of All Neural Network–based Methods

Inputs	Method-1 (Section 3.1) { L , T_{eff} , $\Delta\nu$, ϵ } (%)	Method-2 (Section 3.2) { $\nu_1 - \nu_7$ } (%)	Method-3 (Current Method) { L , T_{eff} , eight modes} (%)
M	99.9	99.5	99.8
Z	99.7	99.5	99.6
$\log \tau$	93	96	98.1

statistics such as the χ^2 averages out small-scale information and hence cannot be used to assess the performance across all the ages. However, a performance-wise comparison after studying Figures 8 and 10 suggest that the outlier level is lower for age inference in Method-3. Hence, we conclude that results from Method-3 are preferred. Nonetheless, Method-1 remains practically applicable until definitive mode identification becomes possible in δ Sct stars.

At present, we were unable to apply this method to measure structure parameters in observed stars as it is challenging to accurately label the dipole modes.

3.3.1. Feature Importance

To understand the importance of the dipole and radial modes, we carried out a feature-importance experiment for these parameters and show the plots in Figure 11.

An important conclusion is that while M and Z do not significantly depend on radial and dipole frequencies, the exact opposite is seen when inferring age. Due to their global nature, L and T_{eff} appear to encode enough information of global parameters M and Z , rendering the oscillation measurements less useful. In contrast, age depends on the deep interior more than the shallow layers since the core hydrogen fraction (X_c) governs the evolution. Since pulsation frequencies are ideal probes of the stellar interior, age determination strongly relies on them.

4. Method 4: Least-square Fitting of Stellar Parameters

Each method described above has its own set of advantages and disadvantages. In this section, we employed a grid-search algorithm to minimize the least-square loss functions in order to identify the model that best matches the observation. This method requires interactive inspection to obtain accurate fits, provided that there exists a close-fit model to the observation. A similar approach was used by Steindl et al. (2022) to fit stellar parameters to a small number of δ Sct stars.

One of the advantages of this method is it can be applied to the 60 stars from Bedding et al. (2020) to achieve good results. Even for stars with missing values of L or T_{eff} , this method can obtain a good fit to observed spectra.

4.1. Method

The method of least squares is a common technique to fit photometric (L), spectroscopic (T_{eff}), and seismic quantities (eigenfrequencies) between observations and models. The underlying principle involves assigning a χ^2 value (as shown in Equation (2)) to each sample in the model, which represents a weighted combination of the squared differences between the observed and model values. The objective is to find the model sample that results in the minimum value of χ^2 . The values of σ_L , $\sigma_{T_{\text{eff}}}$, and σ_{ν_i} are critical parameters in this approach as they

Table 3
Comparing χ^2/N for All the Methods

Inputs	Method-1 (Section 3.1) { L , T_{eff} , $\Delta\nu$, ϵ }	Method-2 (Section 3.2) { $\nu_1 - \nu_7$ }	Method-3 (Current Method) { L , T_{eff} , eight modes}
M	7×10^{-5}	10^{-5}	2×10^{-6}
Z	10^{-7}	5×10^{-8}	9×10^{-9}
$\log \tau$	3×10^{-3}	6.5×10^{-4}	10^{-3}

represent the magnitude of the errors that can be tolerated. This methodology can be highly effective if the appropriate σ values are used:

$$\chi^2 = \left\{ \frac{(L_{\text{obs}} - L_{\text{model}})^2}{\sigma_L^2} + \frac{(T_{\text{eff,obs}} - T_{\text{eff,model}})^2}{\sigma_{T_{\text{eff}}}^2} + \sum_{i=1}^N \frac{(\nu_{i,\text{obs}} - \nu_{i,\text{model}})^2}{\sigma_{\nu_i}^2} \right\}. \quad (2)$$

The last part of Equation (2) indicates the requirement of determining both the observed ($\nu_{i,\text{obs}}$) and model frequencies ($\nu_{i,\text{model}}$) of the same radial order and angular degree. However, accurately identifying and labeling the observed modes in δ Sct stars is challenging due to the high density contamination and missing modes as well as presence of modes with unknown origin. Identification of genuine modes requires iterative pre-whitening followed by elimination of frequency combinations—which adds to the complexity of the fitting routine.

In our approach, we have made slight modifications to a similar method. Our primary objective is to search for a model that can reproduce as many observed modes as possible without having additional spurious peaks. We have applied constraints to the models using the observed values of $\Delta\nu$ (which are obtained from Bedding et al. 2020) to prevent selection of erroneous fits—since a model with much lower $\Delta\nu$ can accurately match a relatively large number of significant observed modes. Finally, we introduce a χ^2 term to compare few observed frequencies to their nearest model frequencies ($\nu_{\text{model}}^{\text{closest}}$). Our modified χ^2 looks like Equation (3):

$$\chi^2 = \left\{ \frac{(L_{\text{obs}} - L_{\text{model}})^2}{\sigma_L^2} + \frac{(T_{\text{eff,obs}} - T_{\text{eff,model}})^2}{\sigma_{T_{\text{eff}}}^2} + \frac{(\Delta\nu_{\text{obs}} - \Delta\nu_{\text{model}})^2}{\sigma_{\Delta\nu}^2} + \sum_{\nu_1}^{\nu_N} \frac{(\nu_{\text{obs}} - \nu_{\text{model}}^{\text{closest}})^2}{\sigma_{\nu}^2} \right\}. \quad (3)$$

The χ^2 formula therefore has similarity to that of Steindl et al. (2022) and the likelihood function of Scutt et al. (2023).

Values of σ_L have been taken from Bedding et al. (2020). Following the same, we have set the uncertainty in T_{eff} to be 2% and that of $\Delta\nu$ to be 0.02 d^{-1} . The Rayleigh frequency resolution criterion has been taken as the uncertainty in mode frequencies, similar to Steindl et al. (2022). Since we fitted three parameters simultaneously (M , Z , τ), 1σ uncertainties (or 68% confidence interval) associated with the best-fit parameters correspond to a 3.5 increase from χ_{min}^2 (Table 1 of Avni 1976).

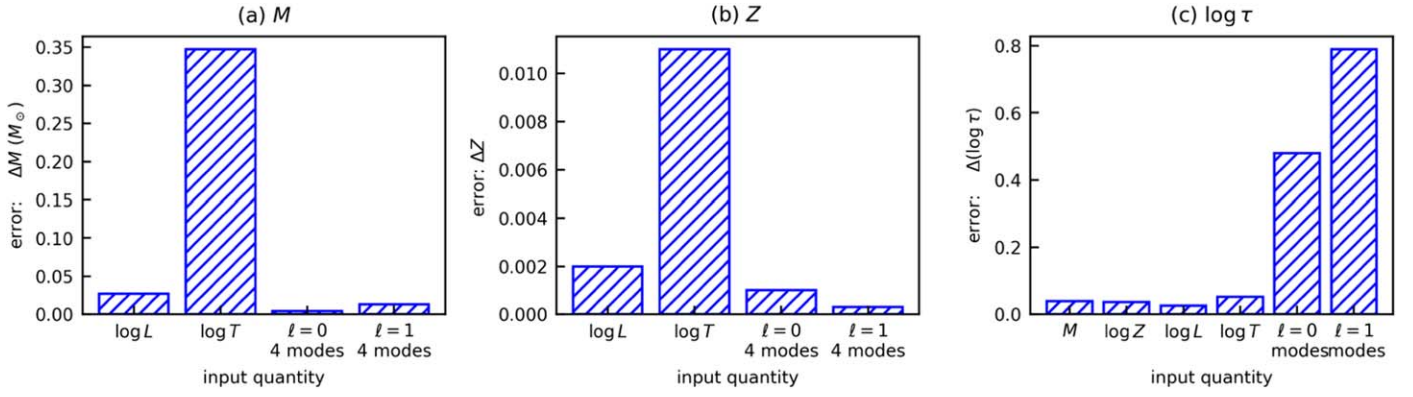


Figure 11. Qualitative contributions arising from input quantities for inferences of (a) M , (b) Z , and (c) $\log \tau$.

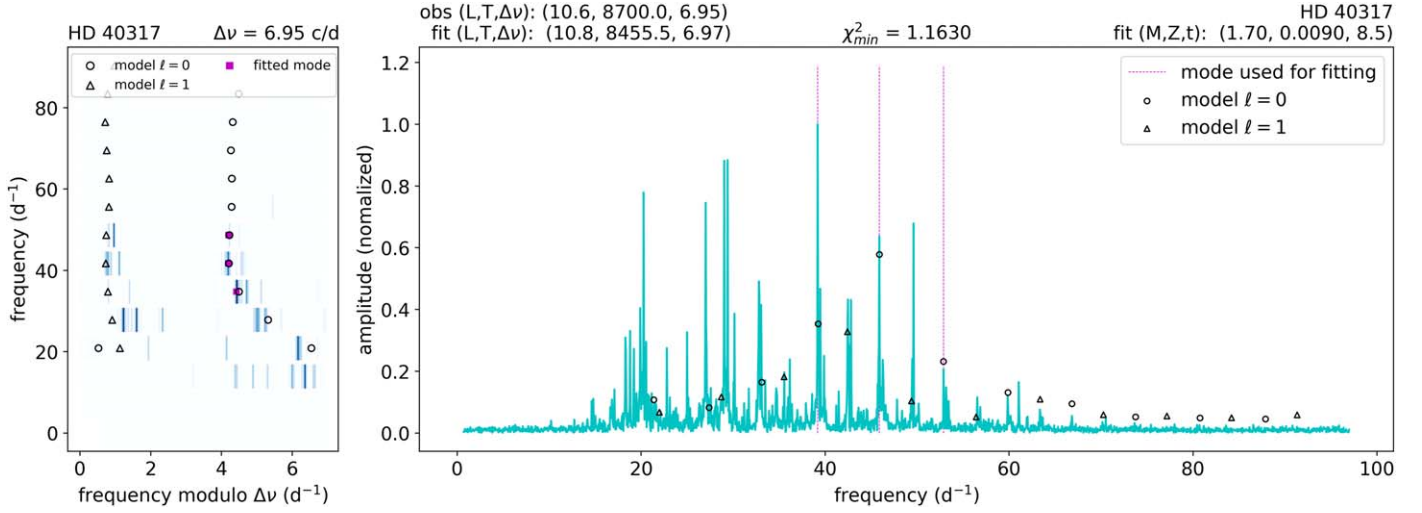


Figure 12. Obtaining a best-fit model to observation of HD 40317. The dotted lines on the right side spectrum shows the three modes we selected for the fitting routine. These three modes are also shown in the échelle diagram (on left) as filled rectangle symbols. After determining the best-fit model, we show its radial and dipole modes as open circles and triangles over both the échelle diagram and the oscillation spectrum. Some of these open symbols do not exactly fall on the observed modes because the fitted frequencies fall within the spectral windows in the vicinity of the sharp peaks. We also report the observed and best-fit values of L , T_{eff} , and $\Delta\nu$ in the title of the spectrum plot. The (M, Z, τ) values of the best-fit model are presented in the same title.

(The complete figure set (60 images) is available.)

Hence we assembled all the model parameters corresponding to $\chi^2 \in [\chi_{\text{min}}^2, \chi_{\text{min}}^2 + 3.5]$ and used their spread to calculate the uncertainties.

Regarding the frequency component of χ^2 , we neither calculated eigenfrequencies from iterative pre-whitening nor assigned any possible identifications to the peaks. Instead, we visually inspected the spectrum and started by selecting four peaks of relatively high frequency and significant amplitudes. We selected these modes through trial and error. After beginning with this arbitrary set of mode we searched for their closest eigenfrequencies ($\nu_{\text{model}}^{\text{closest}}$) across all the model samples disregarding their n or ℓ . Treating these frequencies as inputs to Equation (3), we calculated χ^2 across all the models and inspected for χ_{min}^2 . We repeatedly selected different sets of input frequencies as well as varied the number of fitted modes ($N=1, 2, 3, 4$, rarely 5) and carried out the entire fitting process afresh until we achieved a minimum possible χ_{min}^2 . Finally, we also constructed an échelle diagram to ensure that the N selected modes were genuine $m=0$ frequencies and the obtained solution was able to fit other significant radial and dipole modes as well. Hence, we used the échelle diagrams to

confirm that we are not comparing model modes with incorrect peaks such as rotational splits, combination frequencies, etc.

The reason we favored selecting very few modes is as follows. It is not always possible to obtain exact fits to all the observed modes simultaneously. In such scenarios, fitting larger numbers of modes would demand a highly sophisticated mode-selection process since we are picking up the modes that are able to be modeled through trial and error. Inappropriate mode selection usually leads to a solution where none of the modes are comparable to the observed modes. However, for each star, we were successful in identifying a smaller number of genuine modes, which, using as hinge points, we could fit a (mass, metallicity, age) solution that was finally able to fit most of the observed modes in the entire spectra.

This fitting routine takes us ~ 10 s given that we vectorized this operation across 112 cpu cores using NumPy. Otherwise, this would correspond to ~ 20 cpu minutes (per single star) without any core-level parallelization. However the mode-selection process (being manual and interactive) is the most difficult one, and it took us around 10 minutes per single star.

Table 4
Inferred Values of Mass, Composition, and Age of 60 δ Sct Stars Taken from Bedding et al. (2020)

Id	mass (M_{\odot})	Z_i	age (Myr)
HD 2280	1.35 $^{+0.1}_{-0.05}$	0.008 $^{+0.001}_{-0.002}$	977.7 $^{+202.9}_{-1.23}$
HD 3622	1.7 $^{+0.05}_{-0.15}$	0.022 $^{+0.002}_{-0.014}$	50.6 $^{+75.3}_{-42.04}$
HD 10779	1.6 $^{+0.1}_{-0.02}$	0.009 $^{+0.013}_{-0.001}$	9.0 $^{+156.43}_{-0.25}$
HD 17341	1.65 $^{+0.1}_{-0.01}$	0.012 $^{+0.006}_{-0.001}$	9.0 $^{+2.67}_{-0.01}$
HD 17693	1.7 $^{+0.05}_{-0.05}$	0.012 $^{+0.001}_{-0.003}$	9.7 $^{+0.01}_{-1.59}$
HD 20203	1.5 $^{+0.04}_{-0.05}$	0.008 $^{+0.001}_{-0.001}$	692.5 $^{+0.06}_{-132.78}$
HD 20232	1.68 $^{+0.02}_{-0.13}$	0.018 $^{+0.001}_{-0.011}$	229.8 $^{+194.08}_{-221.47}$
HD 24572	1.52 $^{+0.06}_{-0.02}$	0.013 $^{+0.003}_{-0.004}$	344.0 $^{+132.62}_{-331.75}$
HD 24975	1.7 $^{+0.05}_{-0.06}$	0.014 $^{+0.001}_{-0.003}$	10.4 $^{+0.6}_{-1.55}$
HD 25674	1.54 $^{+0.01}_{-0.04}$	0.007 $^{+0.001}_{-0.001}$	829.4 $^{+77.82}_{-0.08}$
HD 28548	1.7 $^{+0.05}_{-0.06}$	0.012 $^{+0.001}_{-0.006}$	163.0 $^{+158.0}_{-155.63}$
HD 30422	1.5 $^{+0.02}_{-0.05}$	0.006 $^{+0.001}_{-0.001}$	8.3 $^{+0.01}_{-0.01}$
HD 31322	1.75 $^{+0.05}_{-0.05}$	0.011 $^{+0.001}_{-0.002}$	7.7 $^{+0.01}_{-0.75}$
HD 31640	1.55 $^{+0.09}_{-0.03}$	0.009 $^{+0.004}_{-0.001}$	9.3 $^{+2.44}_{-0.23}$
HD 31901	1.58 $^{+0.06}_{-0.02}$	0.009 $^{+0.001}_{-0.001}$	9.4 $^{+0.01}_{-0.58}$
HD 32433	1.62 $^{+0.03}_{-0.1}$	0.018 $^{+0.002}_{-0.01}$	201.1 $^{+193.23}_{-191.66}$
HD 38597	1.58 $^{+0.06}_{-0.02}$	0.008 $^{+0.002}_{-0.001}$	694.8 $^{+0.02}_{-185.18}$
HD 38629	1.45 $^{+0.05}_{-0.1}$	0.004 $^{+0.001}_{-0.001}$	972.4 $^{+0.21}_{-0.86}$
HD 40317	1.7 $^{+0.05}_{-0.08}$	0.009 $^{+0.001}_{-0.002}$	8.5 $^{+0.16}_{-1.17}$
HD 42005	1.6 $^{+0.02}_{-0.01}$	0.008 $^{+0.001}_{-0.001}$	8.6 $^{+0.01}_{-0.01}$
HD 42608	1.75 $^{+0.05}_{-0.1}$	0.018 $^{+0.002}_{-0.01}$	13.8 $^{+96.09}_{-5.7}$
HD 44726	1.55 $^{+0.01}_{-0.03}$	0.011 $^{+0.001}_{-0.003}$	396.6 $^{+253.75}_{-383.59}$
HD 44930	1.64 $^{+0.01}_{-0.1}$	0.018 $^{+0.008}_{-0.005}$	13.7 $^{+453.78}_{-3.78}$
HD 44958	1.6 $^{+0.1}_{-0.02}$	0.009 $^{+0.013}_{-0.001}$	9.1 $^{+11.22}_{-0.05}$
HD 45424	1.55 $^{+0.01}_{-0.03}$	0.008 $^{+0.001}_{-0.001}$	823.0 $^{+54.73}_{-0.06}$
HD 46722	1.52 $^{+0.01}_{-0.02}$	0.008 $^{+0.001}_{-0.001}$	9.1 $^{+0.27}_{-0.01}$
HD 48985	1.64 $^{+0.04}_{-0.02}$	0.008 $^{+0.001}_{-0.001}$	8.5 $^{+0.01}_{-0.67}$
HD 50153	1.7 $^{+0.05}_{-0.02}$	0.02 $^{+0.002}_{-0.002}$	15.9 $^{+0.01}_{-0.01}$
HD 54711	1.62 $^{+0.06}_{-0.12}$	0.009 $^{+0.006}_{-0.003}$	9.8 $^{+378.22}_{-1.95}$
HD 55863	1.64 $^{+0.01}_{-0.06}$	0.009 $^{+0.001}_{-0.001}$	8.6 $^{+0.69}_{-0.09}$
HD 59104	1.56 $^{+0.02}_{-0.02}$	0.018 $^{+0.002}_{-0.002}$	19.1 $^{+297.27}_{-1.96}$
HD 59594	1.6 $^{+0.05}_{-0.1}$	0.015 $^{+0.005}_{-0.007}$	13.9 $^{+476.0}_{-4.77}$
HD 78198	1.62 $^{+0.06}_{-0.02}$	0.014 $^{+0.006}_{-0.001}$	9.9 $^{+4.74}_{-0.37}$
HD 99506	1.65 $^{+0.03}_{-0.1}$	0.018 $^{+0.002}_{-0.01}$	16.2 $^{+246.96}_{-7.1}$
HD 223011	1.62 $^{+0.18}_{-0.02}$	0.01 $^{+0.014}_{-0.001}$	8.7 $^{+438.49}_{-0.32}$
HD 290799	1.55 $^{+0.01}_{-0.01}$	0.004 $^{+0.001}_{-0.001}$	7.1 $^{+0.01}_{-0.93}$
TIC 349645354	1.75 $^{+0.05}_{-0.05}$	0.024 $^{+0.002}_{-0.004}$	12.3 $^{+0.01}_{-2.14}$
TIC 431695696	1.54 $^{+0.08}_{-0.04}$	0.006 $^{+0.002}_{-0.001}$	8.1 $^{+1.14}_{-0.01}$
TIC 124381332	1.68 $^{+0.07}_{-0.06}$	0.014 $^{+0.001}_{-0.007}$	13.3 $^{+145.36}_{-5.31}$
TIC 340358522	1.62 $^{+0.02}_{-0.02}$	0.008 $^{+0.001}_{-0.001}$	8.4 $^{+0.01}_{-0.01}$
HD 187547	1.58 $^{+0.02}_{-0.04}$	0.018 $^{+0.002}_{-0.002}$	177.9 $^{+0.64}_{-160.44}$
KIC 8415752	1.75 $^{+0.05}_{-0.05}$	0.024 $^{+0.002}_{-0.002}$	344.6 $^{+0.04}_{-0.02}$
KIC 9450940	1.62 $^{+0.03}_{-0.02}$	0.015 $^{+0.001}_{-0.001}$	702.5 $^{+53.63}_{-51.24}$
HD 37286	1.52 $^{+0.06}_{-0.02}$	0.006 $^{+0.005}_{-0.001}$	8.5 $^{+4.51}_{-0.01}$
HD 39060	1.45 $^{+0.05}_{-0.1}$	0.008 $^{+0.001}_{-0.001}$	861.4 $^{+0.45}_{-0.53}$
HD 42915	1.55 $^{+0.09}_{-0.01}$	0.006 $^{+0.001}_{-0.001}$	7.6 $^{+0.01}_{-0.87}$
HD 290750	2.1 $^{+0.1}_{-0.1}$	0.013 $^{+0.013}_{-0.001}$	5.8 $^{+185.38}_{-0.03}$
TIC 143381070	1.5 $^{+0.02}_{-0.05}$	0.007 $^{+0.001}_{-0.001}$	594.4 $^{+0.03}_{-117.6}$
TIC 260161111	1.54 $^{+0.06}_{-0.04}$	0.008 $^{+0.002}_{-0.003}$	599.3 $^{+51.98}_{-591.2}$
HD 10961	1.35 $^{+0.1}_{-0.05}$	0.003 $^{+0.001}_{-0.001}$	8.4 $^{+0.01}_{-0.01}$
HD 25248	1.5 $^{+0.02}_{-0.05}$	0.009 $^{+0.005}_{-0.001}$	10.9 $^{+4.14}_{-0.01}$
HD 67688	1.68 $^{+0.02}_{-0.03}$	0.008 $^{+0.001}_{-0.001}$	7.6 $^{+0.01}_{-0.01}$
HD 70510	1.65 $^{+0.03}_{-0.01}$	0.018 $^{+0.002}_{-0.002}$	90.0 $^{+0.12}_{-74.06}$
HD 75040	1.6 $^{+0.02}_{-0.05}$	0.011 $^{+0.001}_{-0.001}$	10.0 $^{+0.58}_{-0.09}$
HD 222496	1.8 $^{+0.05}_{-0.15}$	0.022 $^{+0.002}_{-0.009}$	12.1 $^{+485.56}_{-3.64}$
HD 34282	1.6 $^{+0.02}_{-0.1}$	0.009 $^{+0.001}_{-0.004}$	421.4 $^{+390.4}_{-0.02}$

Table 4
(Continued)

Id	mass (M_{\odot})	Z_i	age (Myr)
HD 29783	1.68 $^{+0.02}_{-0.04}$	0.009 $^{+0.001}_{-0.001}$	8.5 $^{+0.3}_{-0.61}$
HD 220811	1.54 $^{+0.04}_{-0.01}$	0.015 $^{+0.003}_{-0.001}$	849.5 $^{+0.05}_{-154.81}$
HD 25369	1.58 $^{+0.06}_{-0.04}$	0.012 $^{+0.006}_{-0.001}$	9.9 $^{+5.47}_{-0.33}$
HD 89263	1.52 $^{+0.23}_{-0.07}$	0.011 $^{+0.013}_{-0.006}$	561.8 $^{+194.6}_{-555.8}$

Note. These are obtained from the χ^2 minimization method.

In Figure 12, we present an example of our successfully fitted results using this methodology. It was challenging for us to find a close-fit model where lower-order model modes would precisely align with the observed modes. Additionally, dipole modes of the fitted models were sometimes seen to be present in the vicinity of the observed ones but not precisely. This discrepancy could possibly be due to the unequal splitting of dipole modes and the rotation-induced shift of $m=0$ components, even in radial modes.

4.2. Results

In this section, we present the results of our method on 60 stars from Bedding et al. (2020). For three of these stars, either one or both of (L , T_{eff}) inputs were missing. For such stars, we ignored the corresponding contributions of χ^2 . As the best-fit model has an inherent value of missing parameters, one can have a crude estimate of the parameters for these stars.

In Table 4 and Figures A1–A3 of Appendix A, we have presented the fitted structure parameters of the individual stars. Additionally, Figure 13 summarizes the statistics, indicating that most of the fitted masses are approximately $\sim 1.6 M_{\odot}$, while the dominant metallicity values are distributed around $Z=0.010$, corresponding to $[\text{Fe}/\text{H}] \sim -0.146$. We also observed a bimodal age distribution among the stars, where more than half of them are young (around ~ 10 Myr) and a few are very old (over 100 Myr). However, we emphasize that age inferences are not highly precise due to the degeneracy effect, which means that at two different ages, the star can have similar physical and seismic structure.

5. Conclusion

We have deployed a least-squares minimization technique to obtain the structure parameters of 60 δ Sct stars that show regular p -mode pulsation patterns. This method allows us to carry out spectrum fitting without prior mode identification. It is semi-automated in the sense that we fit very few modes in the trial-and-error effort, and mode identification comes as a by-product of the fitting routine. We provided the first inferences of M , Z ($[\text{Fe}/\text{H}]$) and age (τ) for these stars.

We found the masses of most of these stars to be distributed around $1.6 M_{\odot}$, with the exception of two stars of lower mass (HD 2280, HD 10961: $\sim 1.4 M_{\odot}$) and one star with the highest mass (HD 290750: $2.1 M_{\odot}$). Metallicity of a significant fraction of the stars are found to hover around $Z=0.010$ (or $[\text{Fe}/\text{H}] = -0.23$). In this sample, we also found a few stars having very low as well as very high values of metallicity. TIC 349645354 and KIC 8415752 have the highest metallicity, at $Z=0.024$. Finally, more than half of the stars turned out to be

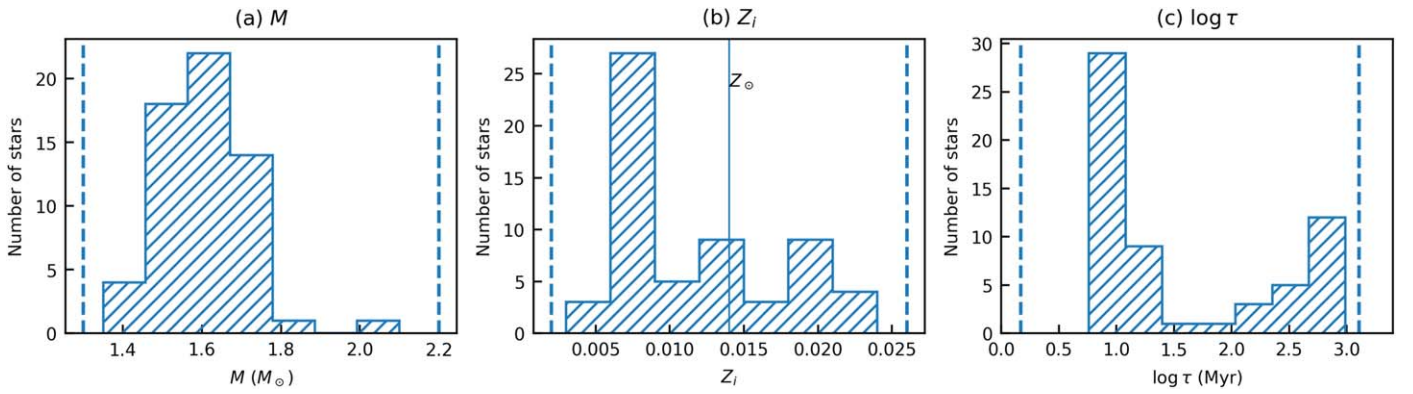


Figure 13. Statistics of the fundamental parameters of 60 δ Sct stars, inferred using the least-squares minimization method. The dotted vertical lines represent the boundary of the model grid.

younger than 30 Myr, with the rest several hundreds of Myr old.

We had originally developed three ML-based neural networks to carry out similar parameter inferences. Although we were unable to obtain reliable results, they still carry the potential of simpler as well as faster parametric fitting. On the synthetic data, our neural networks were able to infer M and Z much more accurately using $\{L, T_{\text{eff}}, \Delta\nu, \epsilon\}$ as inputs. However, age inferences were in general not as accurate as M or Z . This is because, over the course of their MS evolution, stars cross their pre-MS trajectory, which makes *all* their structure parameters degenerate in these two stages of evolution. A similar behavior was demonstrated in Murphy et al. (2021a). Therefore, age inference is not expected to be confident.

With the exception of the parameter inference, neural networks allowed us to carry out an additional analysis—we were able to determine the relative importance of different input quantities. We determined that T_{eff} plays a critical role in the inference of all parameters. ϵ was found to have significance as important as $\log Z$ and other parameters like M , $\Delta\nu$, and L while constraining the age.

We observed that a longer pattern of radial modes (starting from $n = 1$) contains critical information about δ Sct structure. This set of frequencies may be treated as an essential substitute to $\{L, T_{\text{eff}}\}$ as we found that they can constrain stellar parameters even without L and T_{eff} . Doing the feature-importance experiment, we found that ν_6 , ν_2 , and ν_3 are the most significant radial modes.

Finally, we noticed that inclusion of dipole modes led to more precise determination of δ Sct age. We used L , T_{eff} , and frequencies of both radial ($\ell = 0$) and dipole ($\ell = 1$) modes with radial order $n \in [4-7]$ as inputs to infer different parameters. The degeneracy problem in age was reduced while using these inputs. We therefore conclude that dipole modes act as independent quantities with which to constrain stellar parameters, and they add supplementary information to radial modes and $\{\Delta\nu, \epsilon\}$.

Our models lack the implementation of rotation and gravity darkening—which have significant impacts over stellar evolution and pulsation. While 5 km s^{-1} fluctuation in rotation velocity can perturb the pulsation frequencies by 2%–3%

(Deupree 2011), gravity darkening can cause as high as $\sim 50\%$ and 2.5% departures in L and T_{eff} (Paxton et al. 2019) respectively. Depending on these facts, our parameter inferences can be subject to modification once we introduce such phenomena. However, this is beyond our current scope, and we look forward to studying their impacts in a future project. Such a detailed analysis will help us in putting more realistic constraints over the ages of multiple δ Sct stars observed in missions like TESS and Kepler.

Acknowledgments

S.D. acknowledges SERB, DST, Government of India, C II and Intel Technology India Pvt. Ltd. for the Prime Minister’s fellowship and facilitating research. We have performed all computations in the Intel Lab Academic Compute Environment using Intel® Xeon® Platinum 8280 CPU. MESA (Paxton et al. 2010) and GYRE (Townsend et al. 2013) codes have been very useful in simulating the data, without which this project would not have been possible. We have used Python packages like SciPy (Oliphant 2007), Matplotlib (Hunter 2007), NumPy (van der Walt et al. 2011), Keras (Chollet et al. 2015), and Tensorflow (Abadi et al. 2015). This research made use of Lightkurve (Lightkurve Collaboration et al. 2018), a Python package for Kepler and TESS data analysis. GNU parallel (Tange 2011) has been used to do parallel computation. S.J.M. was supported by the Australian Research Council (ARC) through Future Fellowship FT210100485. T.R.B. was also supported by the ARC, through DP210103119 and FL220100117, and by the Danish National Research Foundation (grant D NRF106) through its funding for the Stellar Astrophysics Centre (SAC). We thank Antonio García Hernández for suggestions regarding the impacts of rotation and gravity darkening. Finally we are thankful to the referee for very useful comments.

Appendix A Inference for Each Star

We show below in Figures A1–A3, M , Z , and τ inferences from Method-4 for 60 δ Sct stars taken from Bedding et al. (2020). The x -axis contains the IDs of the stars and the y -axis displays the inferred quantities.

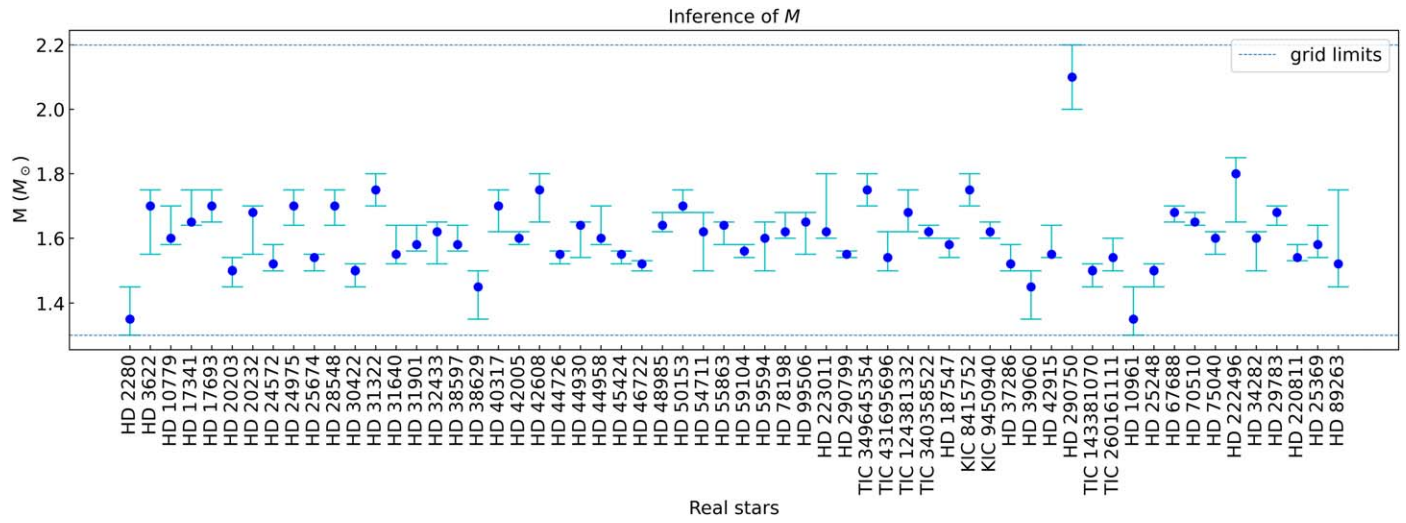


Figure A1. M inference for 60 δ Scuti stars.

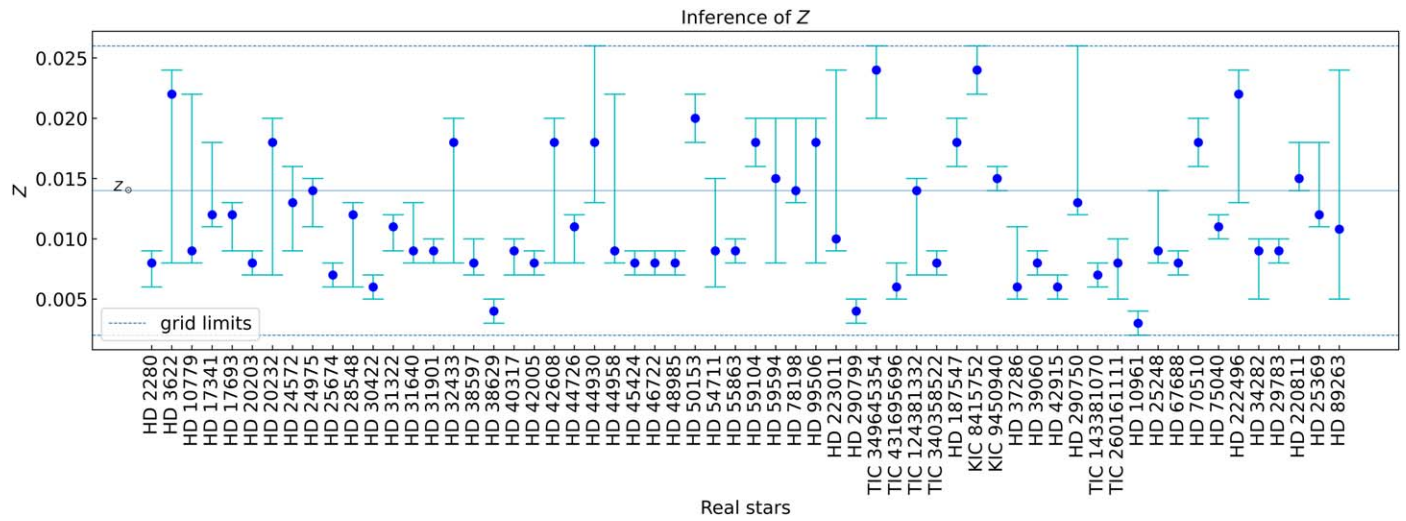


Figure A2. Z inference for 60 δ Scuti stars.

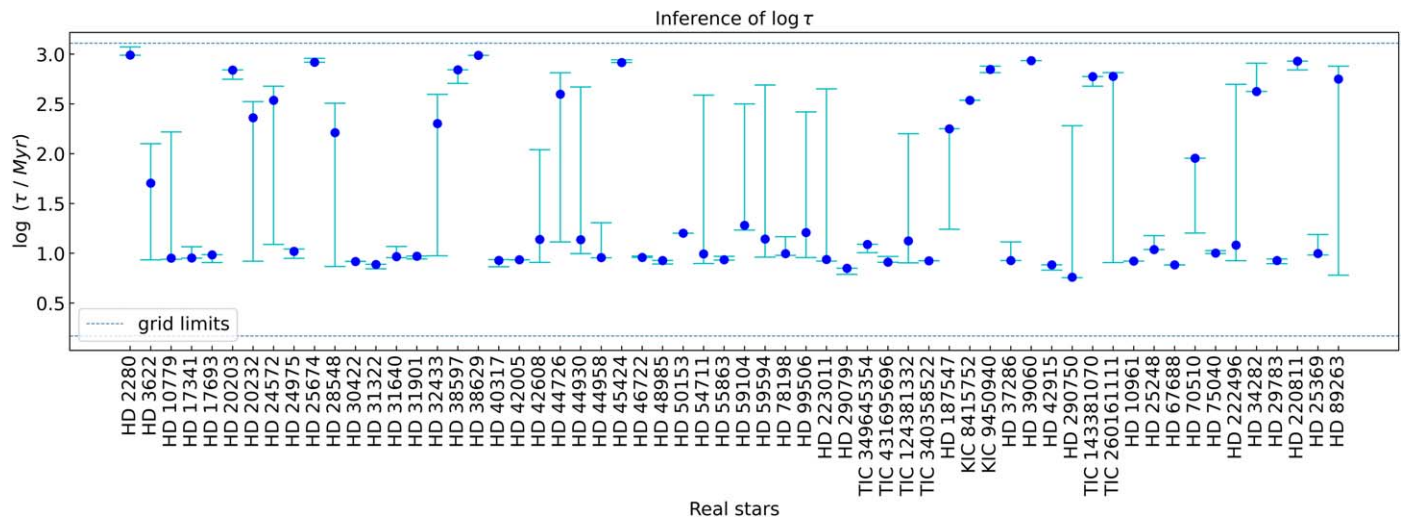


Figure A3. $\log_{10}(\tau/\text{Myr})$ inference for 60 δ Scuti stars.

Appendix B Group-wise Inference Accuracy

For most of the stars, measured values of L and T_{eff} are available although these quantities are not sufficient to constrain different stellar parameters. Additional independent quantities are expected to assist in constraining these structure parameters.

Asteroseismic quantities $\Delta\nu$ and ϵ are suitable for this purpose. But neither (L, T_{eff}) nor $(\Delta\nu, \epsilon)$ alone can accurately infer the stellar parameters. However, when combined, these parameters can efficiently constrain those stellar parameters.

We considered $\{L, T_{\text{eff}}, R\}$ as inputs, trained the networks with these, and measured the maximum absolute errors between true values and network predictions (over the validation samples). Similarly, we took asteroseismic quantities $\{\Delta\nu, \epsilon\}$ and repeated this validation process. Finally, we combined all of them and again measured the maximum absolute error associated with the predictions. During age inference, we supplemented M, Z -like quantities and also assembled the values of validation errors. We visualize all of these errors in Figure B1, which emphasizes that validation error decreases drastically when observables and asteroseismic quantities are simultaneously considered as inputs.

In Table B1, we show the Pearson r correlation coefficients (Rodgers et al. 1988) between network predictions (over validation samples) and corresponding true values. It is a measure of inference accuracy, i.e., correlation between true

Table B1
Pearson R Correlation Coefficients between Inference and True Values for Different Input Sets

	$\{L, T_{\text{eff}}\}$	$\{\Delta\nu, \epsilon\}$	$\{L, T_{\text{eff}}, \Delta\nu, \epsilon\}$	$\{L, T_{\text{eff}}, \Delta\nu, \epsilon, M, Z\}$
M	0.93	0.86	0.99	...
$\log Z$	0.77	0.85	0.99	...
$\log \tau$	0.67	0.78	0.98	0.99

and inferred values. The Pearson r coefficient can have values between -1 and $+1$. The higher the r coefficient, the higher the correlation between true values and network prediction. This Pearson r correlation coefficient between the two sets of measurements $\{p\}$ and $\{q\}$ is calculated by Equation (B1):

$$R = \frac{\sum_i (p_i - \bar{p})(q_i - \bar{q})}{\sqrt{\sum_i (p_i - \bar{p})^2 \sum_i (q_i - \bar{q})^2}}, \quad (\text{B1})$$

where \bar{p}, \bar{q} are the means of the measurements.

Adding (M, Z) as additional inputs increases the Pearson r coefficient by only 0.01. However, from Figure B1(c), it is evident that (M, Z) inputs actually assist in reducing the absolute error associated with $\log \tau$ prediction.

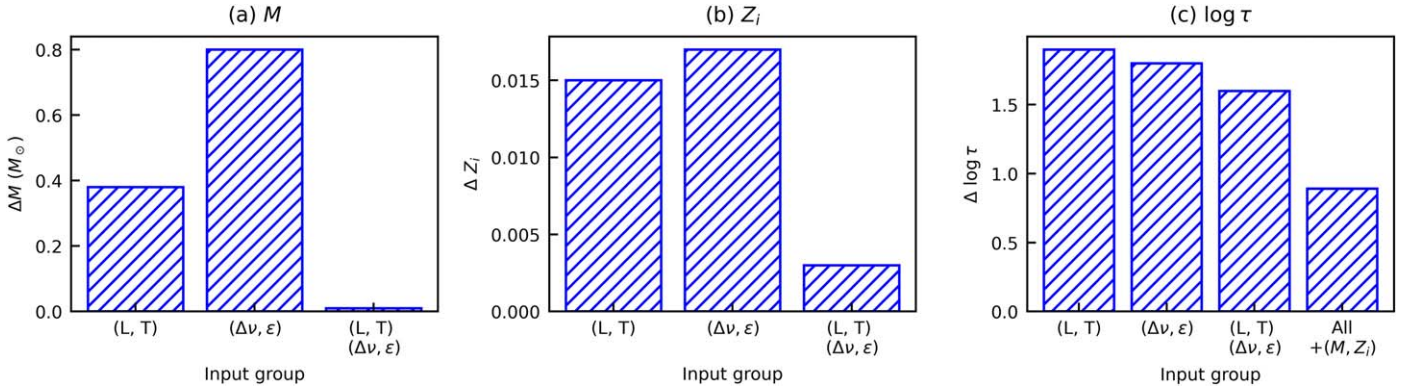


Figure B1. Maximum absolute errors between network prediction and true values for a different group of input quantities shown in the x -axis. Figures for prediction of (a) M in M_{\odot} , (b) Z , and (c) $\log \tau$, where τ is in Myr.

ORCID iDs

Siddharth Dhanpal  <https://orcid.org/0000-0001-8699-3952>
 Simon J. Murphy  <https://orcid.org/0000-0002-5648-3107>
 Shравan Hanasoge  <https://orcid.org/0000-0003-2896-1471>
 Timothy R. Bedding  <https://orcid.org/0000-0001-5222-4661>

References

- Abadi, M., Agarwal, A., Barham, P., et al. 2016, arXiv:1603.04467
- Aerts, C. 2021, *RvMP*, **93**, 015001
- Avni, Y. 1976, *ApJ*, **210**, 642
- Barceló Forteza, S., Moya, A., Barrado, D., et al. 2020, *A&A*, **638**, A59
- Barceló Forteza, S., Roca Cortés, T., García Hernández, A., & García, R. A. 2017, *A&A*, **601**, A57
- Bedding, T. R., Murphy, S. J., Hey, D. R., et al. 2020, *Natur*, **581**, 147
- Bellinger, E. P., Angelou, G. C., Hekker, S., et al. 2016, *ApJ*, **830**, 31
- Borucki, W. J., Koch, D., Basri, G., et al. 2010, *Sci*, **327**, 977
- Bowman, D. M. 2020, *FrASS*, **7**, 70
- Bowman, D. M., Kurtz, D. W., et al. 2018, *MNRAS*, **476**, 3169
- Chaplin, W. J., Miglio, A., et al. 2013, *ARA&A*, **51**, 353
- Chevalier, C. 1971, *A&A*, **14**, 24
- Chollet, F., et al. 2015 Keras, <https://keras.io>
- Deupree, R. G. 2011, *ApJ*, **742**, 9
- Dhanpal, S., Benomar, O., Hanasoge, S., et al. 2022, *ApJ*, **928**, 188
- Dziembowski, W., Krolnikowska, M., et al. 1990, *AcA*, **40**, 19
- García Hernández, A., Moya, A., Michel, E., et al. 2009, *A&A*, **506**, 79
- García Hernández, A., Suárez, J. C., Moya, A., et al. 2017, *MNRAS: Lett.*, **471**, L140
- Garrido, R., Garcia-Lobo, E., & Rodriguez, E. 1990, *A&A*, **234**, 262
- Goldstein, J., Townsend, R. H. D., et al. 2020, *ApJ*, **899**, 116
- Guzik, J. A. 2021, *FrASS*, **8**, 55
- Hasanzadeh, A., Safari, H., & Ghasemi, H. 2021, *MNRAS*, **505**, 1476
- Hekker, S., & Christensen-Dalsgaard, J. 2017, *A&ARv*, **25**, 1
- Hendriks, L., Aerts, C., et al. 2019, *PASP*, **131**, 108001
- Hon, M., Stello, D., Yu, J., et al. 2017, *MNRAS*, **469**, 4578
- Hon, M., Stello, D., Yu, J., et al. 2018, *MNRAS*, **476**, 3233
- Hunter, J. D. 2007, *CSE*, **9**, 90
- Kahraman Alıçavuş, F., Handler, G., Alıçavuş, F., et al. 2022, *MNRAS*, **510**, 1413
- Kingma, D. P., & Ba, J. 2014, arXiv:1412.6980
- Kurtz, D. W. 2022, *ARA&A*, **60**, 31
- Le Dizès, C., Rieutord, M., & Charpinet, S. 2021, *A&A*, **653**, A26
- Li, G., Reeth, T. V., Bedding, T. R., et al. 2019, *MNRAS*, **491**, 3586
- Lightkurve Collaboration, Cardoso, J. V. d. M., Hedges, C., et al., 2018, Lightkurve: Kepler and TESS time series analysis in Python, Astrophysics Source Code Library, ascl:1812.013
- Matthews, J. M. 2007, *CoAst*, **150**, 333
- McNamara, D. H., Clementini, G., Marconi, M., et al. 2007, *AJ*, **133**, 2752
- Mombarg, J. S. G., Reeth, T. V., Aerts, A., et al. 2021, *A&A*, **650**, A58
- Montavon, G., Samek, W., & Müller, K.-R. 2018, *DSP*, **73**, 1
- Mosteller, F., & Tukey, J. 1968, Handbook of Social Psychology, Vol. 2 (Addison-Wesley: Addison-Wesley)
- Moya, A., Suárez, J. C., García Hernández, A., & Mendoza, M. A. 2017, *MNRAS*, **471**, 2491
- Murphy, S. J., Bedding, T. R., Gautam, A., & Joyce, M. 2023, *MNRAS*, **526**, 3779
- Murphy, S. J., Bedding, T. R., White, T. R., et al. 2022, *MNRAS*, **511**, 5718
- Murphy, S. J., Joyce, M., Bedding, T. R., White, T. R., & Kama, M. 2021, *MNRAS*, **502**, 1633
- Murphy, S. J., Paunzen, E., Bedding, T. R., Walczak, P., & Huber, D. 2020, *MNRAS*, **495**, 1888
- Oliphant, T. E. 2007, *CSE*, **9**, 10
- Pamos Ortega, D., García Hernández, A., Suárez, J. C., et al. 2022, *MNRAS*, **513**, 374
- Paparó, M. 2019, *FrASS*, **6**, 26
- Paparó, M., Bognár, Zs., Benkő, J. M., et al. 2013, *A&A*, **557**, A27
- Paxton, B., Bildsten, L., Dotter, A., et al. 2010, *ApJS*, **192**, 3
- Paxton, B., Cantiello, M., Arras, P., et al. 2013, *ApJS*, **208**, 4
- Paxton, B., Marchant, P., Schwab, J., et al. 2015, *ApJS*, **220**, 15
- Paxton, B., Schwab, J., Bauer, E., et al. 2018, *ApJS*, **234**, 34
- Paxton, B., Smolec, R., Schwab, J., et al. 2019, *ApJS*, **243**, 10
- Petersen, J. O., & Christensen-Dalsgaard, J. 1996, *A&A*, **312**, 463
- Reese, D., Lignières, F., & Rieutord, M. 2006, *A&A*, **455**, 621
- Ricker, G. R., Winn, J. N., Vanderspek, R., et al. 2014, *JATIS*, **1**, 014003
- Rodgers, J. L., Nicewander, W. A., et al. 1988, *Am. Stat.*, **42**, 59
- Scutt, O. J., Murphy, S. J., Nielsen, M. B., et al. 2023, *MNRAS*, **525**, 5235
- Steindl, T., Zwintz, K., & Müllner, M. 2022, *A&A*, **664**, A32
- Suárez, J. C., García Hernández, A., Moya, A., et al. 2014, *A&A*, **563**, A7
- Tange, O. 2011, 42, login: The USENIX Magazine, 36, 42, Zenodo, doi:10.5281/zenodo.16303
- Townsend, R. H. D., Goldstein, J., Zweibel, E. G., et al. 2017, *MNRAS*, **475**, 879
- Townsend, R. H. D., Teitler, S. A., et al. 2013, *MNRAS*, **435**, 3406
- Uytterhoeven, K., Moya, A., Grigahçène, A., et al. 2011, *A&A*, **534**, A125
- van der Walt, S., Colbert, S. C., & Varoquaux, G. 2011, *CSE*, **13**, 22
- Verma, K., Hanasoge, S., Bhattacharya, J., Antia, H. M., Krishnamurthi, G., et al. 2016, *MNRAS*, **461**, 4206
- Vrard, M., Mosser, B., Samadi, R., et al. 2016, *A&A*, **588**, A87
- Zwintz, K., Lenz, P., Breger, M., et al. 2011, *A&A*, **533**, A133